Phase behavior and implications for travel-time observables (PHASE-2)

Emmanuel Skarsoulis
Foundation for Research and Technology Hellas
Institute of Applied and Computational Mathematics
100 N. Plastira str., GR-70013 Heraklion, Greece
phone: +30-2810-391776 fax: +30-2810-391801
email: eskars@iacm.forth.gr

in collaboration with

Bruce Cornuelle and Matthew Dzieciuch
Scripps Institution of Oceanography
University of California, San Diego
La Jolla, CA 92093-0225
phone: (858) 534-4021 fax: (858) 534-9820
email: bdc@ucsd.edu, mad@uscd.edu

Award Number: N00014-14-1-0616
http://www.iacm.forth.gr, http://sio.ucsd.edu

LONG-TERM GOALS

Our long-term goal is to study the behavior of the wave-theoretic phase in the time domain, in particular its stationarity or non-stationarity, in various propagation conditions and assess the effects on the perturbation behavior of travel time observables due to sound-speed perturbations.

OBJECTIVES

The objective is to study the behavior of the wave-theoretic demodulated phase in the time domain, understand the conditions under which it remains near-stationary or becomes non-stationary, and explain what the effects will be on the perturbation behaviour of peak arrival times and demodulated phase arrival times. The phase behavior is studied in different propagation conditions, short and long-range, deep- and shallow water, range-independent and range-dependent, examining both ray-like and modal arrivals.

APPROACH

The wave-theoretic phase in the time domain is obtained from the inverse Fourier transform of the frequency-domain Green's function calculated using normal-mode theory. In addition, stationary-phase [1] and Taylor-expandion [2,3] approaches are used for approximate fast calculations, but also in order to understand specific aspects of the phase behavior, such as time dependencies and stationarity in the case of ray-like and modal arrivals.

WORK COMPLETED

The motivation for this work came from the results of previous studies, supported by ONR, suggesting that the perturbation behavior of different travel-time observables, peak and demodulated phase arrival times in particular, is similar or dissimilar depending of the behavior, the stationarity/non-stationarity, of the phase along the corresponding arrivals. These dependencies as well as the behavior of the phase in different propagation conditions are addressed in the following.

RESULTS

Phase and travel-time perturbation behavior

The complex pressure at the receiver in the time domain [4] can be written in the form

$$p(t) = a(t)e^{i\varphi(t)}e^{i\omega_0 t}, \tag{1}$$

where t denotes time, $a(t)$ is the amplitude (arrival pattern), $\varphi(t)$ is the phase and ω_0 is the central (carrier) circular frequency of the source. The demodulated pressure

$$\tilde{p}(t) = a(t)e^{i\varphi(t)} = u(t) + iv(t) \tag{2}$$

results after removal of the carrier frequency and can alternatively be expressed in terms of its real and imaginary parts, u and v, respectively. The above quantities $a(t)$, $\varphi(t)$, $u(t)$ and $v(t)$, and the resulting arrival times, depend on the source/receiver location, as well as on the sound-speed distribution $c(\mathbf{x})$, where $\mathbf{x}$ is the spatial variable. Thus, perturbations $\delta c(\mathbf{x})$ give rise to perturbations in arrival amplitude, arrival phase and arrival times.

Peak arrival times $\tau_{P,\ell}$ are defined as the times of the local maxima (peak arrivals) of the arrival pattern, where the index ℓ spans the arrival peaks. As the sound speed changes the peaks of the arrival pattern are deformed and displaced, i.e. peak arrival times change as well. In the following we focus on a single peak and omit the index ℓ for convenience. By applying this definition for the background (c) and perturbed $(c+\delta c)$ state we have

$$\begin{aligned} &\dot{a}(\tau_P; c) = 0, \\ &\dot{a}(\tau_P + \delta\tau_P; c + \delta c) = 0. \end{aligned} \tag{3}$$

where the dots denote time derivatives. A 1st-order Taylor expansion of the left-hand side of the latter about the background state results in

$$\dot{a}(\tau_P; c) + \ddot{a}(\tau_P; c)\delta\tau_P + \delta\dot{a}_1(\tau_P; c; \delta c) = 0 \quad , \tag{4}$$

where $\delta\dot{a}_1$ is the 1st-order perturbation of $\delta\dot{a}$ due to δc. Eq. (4) combined with the background relation in eq. (3) results in

$$\delta\tau_P = -\frac{\delta\dot{a}_1(\tau_P;c;\delta c)}{\ddot{a}(\tau_P;c)} = -\frac{\dot{u}\delta u_1 + u\delta\dot{u}_1 + \dot{v}\delta v_1 + v\delta\dot{v}_1}{\dot{u}^2 + u\ddot{u} + \dot{v}^2 + v\ddot{v}}, \tag{5}$$

where the quantities u, v and their time derivatives are considered at the background state (c) and their 1st-order perturbations are due to δc.

Demodulated phase arrival times τ_{DR} are the times of local maxima (or minima) of u, the real part of the demodulated pressure.

$$\dot{u}(\tau_{DR};c) = 0, \tag{6}$$

Using a similar argument as for the peak arrival time, the perturbation of the phase arrival time τ_{DR} due to a sound speed change can be written as

$$\delta\tau_{DR} = -\frac{\delta\dot{u}_1(\tau_{DR};c;\delta c)}{\ddot{u}(\tau_{DR};c)} \tag{7}$$

At the peak arrival time we have from eq. (3)

$$u\dot{u} + v\dot{v} = 0 \tag{8}$$

The phase $\varphi(t)$ can be written as

$$\varphi(t) = \tan^{-1}\left(\frac{v(t)}{u(t)}\right) \tag{9}$$

And its time derivative can be obtained by differentiation

$$\dot{\varphi} = \frac{u\dot{v} - v\dot{u}}{u^2 + v^2} = \frac{u\dot{v} - v\dot{u}}{a^2} \tag{10}$$

which at the peak arrival time ($t = \tau_P$), through eq. (8), becomes

$$\dot{\varphi} = -\frac{1}{a^2}\left(\frac{u^2\dot{u}}{v} + v\dot{u}\right) = -\frac{\dot{u}}{v} = \frac{\dot{v}}{u} \tag{11}$$

From this relation it follows that if the phase is stationary ($\dot{\varphi} = 0$) at the peak arrival time ($\dot{a} = 0$) then the real and imaginary parts of the demodulated complex pressure u and v are also stationary, i.e. the peak and phase arrival times coincide: $\tau_P = \tau_{DR} = \tau_{DI}$. If the phase is non-stationary ($\dot{\varphi} \neq 0$) at the peak arrival time then the behavior of the peak and demodulated phase arrival times can be different. The phase φ is anticipated to be close to constant (i.e. near stationary) in the case of resolved ray arrivals. If this is the case, peak and demodulated phase arrivals behave similarly.

From the above perturbation relations and assuming range independence vertical sensitivity kernels of the various travel times can be obtained, representing the 1-order effect of sound-speed changes on the corresponding travel-time observables

$$\delta\tau = \int_V K_\tau(z)\delta c(z)dz \tag{12}$$

The similarities and dissimilarities in the perturbation behaviour of the peak and demodulated phase arrivals depending on the stationarity or non-stationarity of the phase are demonstrated in the following.

Fig. 1 shows a linear sound-speed profile typical for the Mediterranean Sea in winter, in a 2500-m deep water layer, followed by an absorbing bottom half space. Both source and receiver are assumed at a depth of 150 m depth

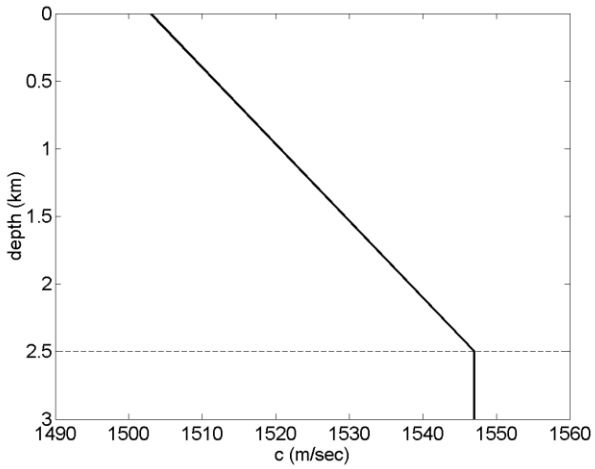

Fig. 1. Linear sound-speed profile, typical for the Mediterranean Sea in winter.

Fig. 2(a) shows the arrival pattern of a Gaussian pulse with central frequency 100 Hz and 3-dB bandwidth 50 Hz at a range of 30 km. The arrival pattern contains six major peaks, the first three of which can be resolved as ray arrivals, i.e. each arrival can be associated with an eigenray. This is not the case for the late arrivals, which are represented by a small number of low-order modes. Two peak arrivals, an early and a late one – marked by crosses and numbered as #1 and #2 in Fig. 2a – are selected to study their sensitivity behavior. Figs. 2(b) and (c) show the real part of the demodulated and the modulated complex pressure at the receiver, respectively. The phase arrivals corresponding to peak arrivals #1 and #2 are also marked on these figures. It is seen that the demodulated phase arrivals correspond, nearly one by one, to the peak arrivals. There are amplitude and sign differences however. (note that Figs. 2(a) and (b) have different vertical scales) . In the modulated pressure, there are multiple cycles for each peak arrival.

Fig. 3(a) shows the phase φ of the received signal as a function of time. The phases corresponding to the selected peak arrival times are marked by crosses. It is seen that the phase is nearly stationary at the early arrival and non-stationary at the late arrival. According to the previous analysis, this implies that the peak and the demodulated phase arrival #1 nearly coincide, whereas there should be differences in

the case of arrival #2. Figs. 3(b) and (c) show the detailed phase changes around peak arrival time #1 and #2. It is seen that the phase of arrival #1 is not strictly stationary – none of the points of stationarity ($\dot{\varphi} = 0$) coincides with the actual peak arrival time #1 (+). The deviation from stationarity is much stronger in the case of arrival #2, Fig. 3(c).

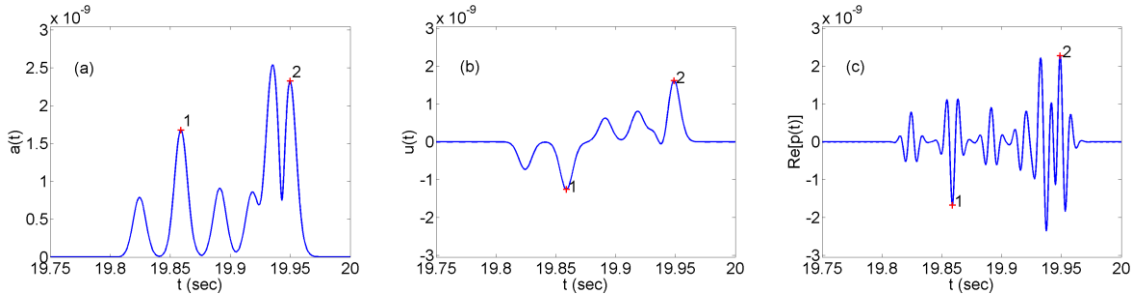

Fig. 2: Arrival pattern (a), real part of demodulated (b) and modulated (c) pressure at 30 km range.

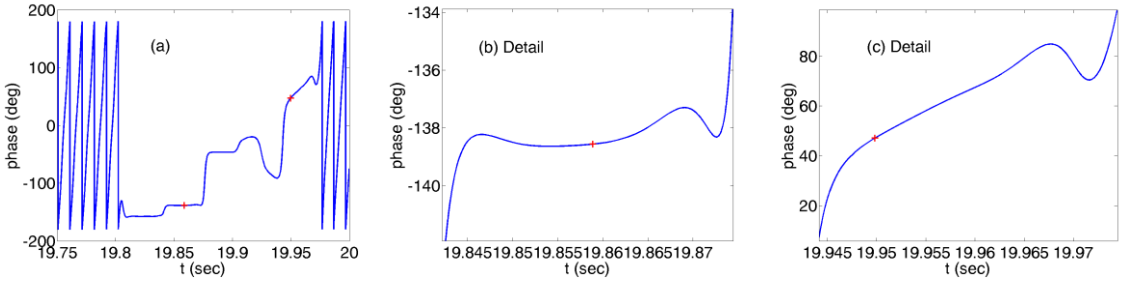

q

Fig. 3: Phase change with time (a) and details for arrivals #1 (b) and #2 (c).

Fig. 4 shows the vertical travel-time sensitivity kernel, normalized by the propagation range, for the peak and demodulated phase arrival time associated with arrival #1 and smoothed with a 100-m moving window. The kernel for the peak arrival time, Fig. 4(a), is comparable, still not identical, with the kernel for the demodulated phase arrival time, Fig. 4(b) and exhibits maximum sensitivity around the lower turning depth – due to the upward refracting sound-speed profile there is no upper turning depth. Fig. 5 shows travel-time perturbations of arrival #1 caused by sound-speed changes about the depth of 1400 m, close to the maximum sensitivity depth, and comparison with the 1st-order predictions based on the corresponding sensitivity kernels. Box-shaped sound-speed perturbations with vertical extent 100 m and magnitude between -0,2 and 0.2 m/sec are considered. The crosses in Fig. 5 represent the actual calculated sound speed perturbations whereas the solid lines show the 1-order predictions from the sensitivity kernels. The predictions turn out to be successful for all three observables. The demodulated phase arrival times appear to be more affected by the sound-speed perturbations than the peak arrival times and further they exhibit a weak non-linear behavior, which cannot be captured by the 1st-order prediction.

Fig. 6 shows the normalized vertical travel-time sensitivity kernel for the peak and phase arrival time associated with arrival #2, again smoothed with a 100-m moving window. The kernels now are limited to sampling a much shallower depth layer. In this case, the kernel for the demodulated phase arrival time is much stronger than the one for the peak arrival time. This is associated with the large deviation

of the phase from stationarity for that particular arrival, Fig. 3(c). Fig. 7 shows travel-time perturbations of arrival #2 caused by sound-speed changes centered about the depth of 150 m, close to the maximum sensitivity depth. Again the sound-speed perturbations are box-shaped with vertical extent 100 m and magnitude between -0.2 and 0.2 m/sec. Even though the sound-speed perturbations are of the same vertical extent and magnitude as before the travel-time perturbations are much larger (note the different vertical scales in Figs. 5 and 7). The predictions based on the sensitivity kernels (solid lines) are in good agreement with the actual travel-time perturbations (crosses) in the case of peak arrival times. The demodulated phase arrival times, Fig. 7(b), exhibit irregular perturbation behavior with strong non-linearity. The 1-order prediction in this case describes the tangent of the actual behavior at the reference state (δc =0).

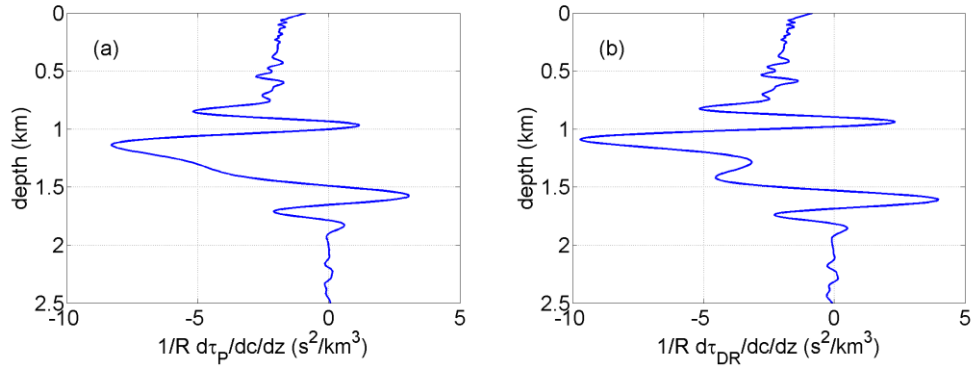

Fig. 4: Vertical sensitivity kernel (a) for peak arrival #1 and (b) for demodulated phase arrival #1

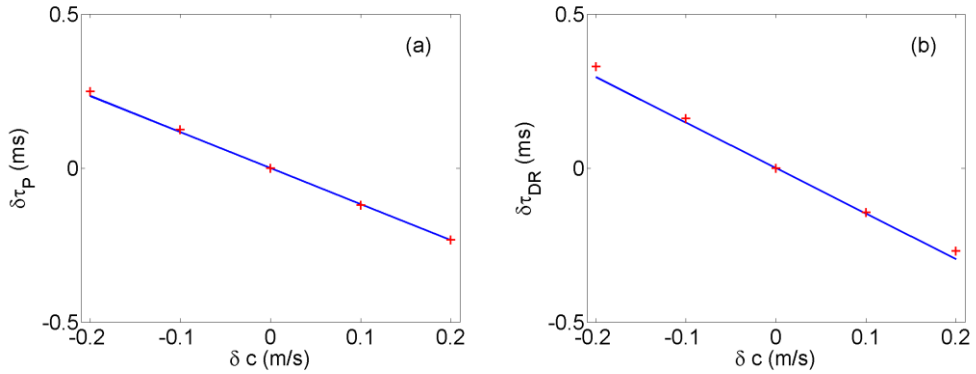

Fig. 5: Actual (+) and predicted (line) travel-time perturbations (a) for peak arrival #1 and (b) for demodulated phase arrival #1

On the basis of these results the similarity or dissimilarity in the perturbation behavior of peak and demodulated phase arrivals appears to be controlled by the time behavior of the phase φ. If the phase at the peak arrival time is close to stationary ($\dot{\varphi} = 0$) the two observables are nearly identical and their perturbation behavior similar. If the phase deviates from stationarity the observables and their sensitivity kernels are different. The larger the deviation the bigger the difference. In the case of resolved ray arrivals (early arrivals in deep-water long-range propagation) the phase turns out to be close to constant, even though not exactly stationary, such that in those cases the difference between peak and demodulated phase arrivals is small, but still not zero. For late arrivals the phase is highly

non-stationary and the differences between the two are large, with the demodulated phase arrivals exhibiting a much higher sensitivity than the peak arrivals as well as non-linearity.

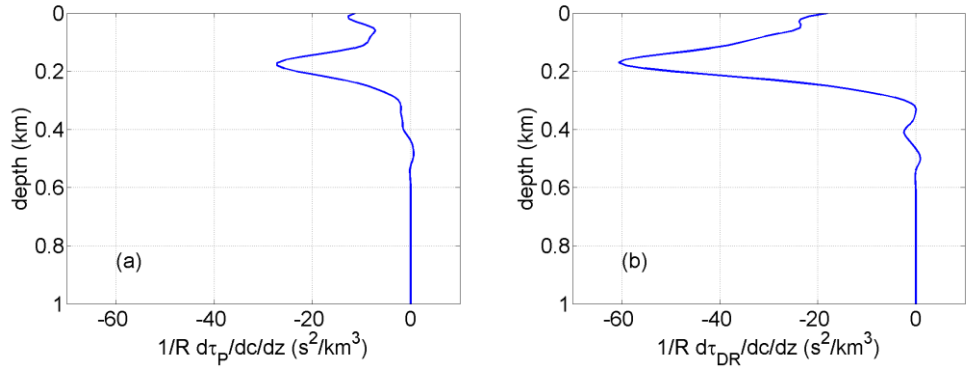

Fig. 6: Vertical sensitivity kernel for peak (a), demodulated (b) and modulated (c) phase arrival #2

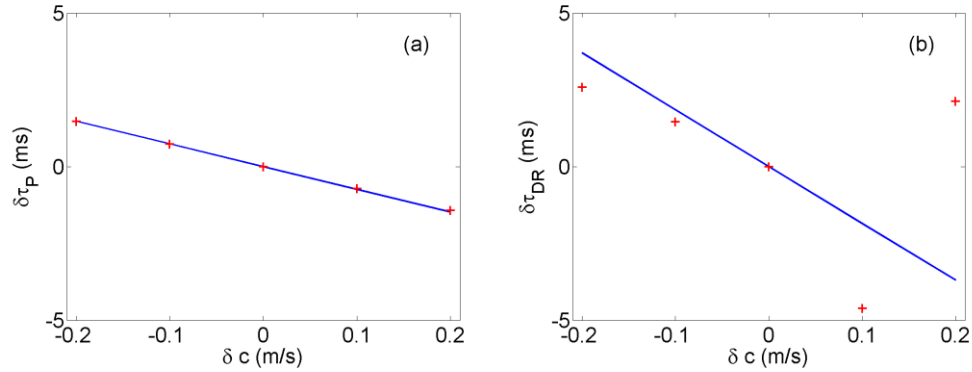

Fig. 7: Actual (+) and predicted (line) travel-time perturbations for arrival #2

Phase behavior of ray-like arrivals

In a range-independent ocean environment characterized by a sound-speed profile $c(z)$ high-order propagating modes interfere with each other and give rise to ray-like arrivals in the time domain, i.e. wave-theoretic arrivals that can be associated with ray arrivals. The double-loop length D of the equivalent eigenray is related to the difference between wavenumbers k_n of subsequent modes [5]

$$\Delta k_n = k_{n+1} - k_n = -\frac{2\pi}{D} \tag{13}$$

The relation (13) is in general fulfilled by different modes at different frequencies within the propagation bandwidth. In a wave-theoretic context the acoustic pressure $p_r(t;c)$ at the receiver in the time domain can be expressed as the inverse Fourier transform of the frequency-domain Green's function $G_{sr}(\omega;c)$, from the source (s) to the receiver (r) multiplied by the spectrum $S(\omega)$ of the emitted signal

$$p_r(t) = \frac{1}{2\pi}\int_{-\infty}^{+\infty} G_{sr}(\omega)S(\omega)e^{i\omega t}d\omega\,. \tag{14}$$

The above acoustic pressure $p_r(t)$ is a complex function of time. Assuming a range-independent environment and large distances from the source, the far-field normal-mode representation of the Green's function can be used

$$G_{sr}(\omega) = \frac{e^{-i\pi/4}}{\sqrt{8\pi}}\sum_{m=1}^{M}\frac{\varphi_m(\omega;z_s)\varphi_m(\omega;z_r)}{\sqrt{k_m(\omega)R}}e^{-ik_m(\omega)R}\,, \tag{15}$$

where φ_m are the propagating modes and k_m the corresponding eigenvalues, R is the horizontal distance between source and receiver, and z_s, z_r their depths. The above expression (15) assumes a harmonic source of unit strength with circular frequency ω and time dependence $e^{i\omega t}$. By substituting the normal-mode representation into eq. (14) the acoustic pressure can be written in the form

$$p_r(t;c) = \frac{e^{-i\pi/4}}{\sqrt{8\pi}}\sum_{m=1}^{M}\int_{-\infty}^{+\infty} S(\omega)\frac{\varphi_m(\omega;z_s)\varphi_m(\omega;z_r)}{\sqrt{k_m(\omega)R}}e^{i(-k_m(\omega)R+\omega t)}d\omega \tag{16}$$

By applying the method of stationary phase for the evaluation of the Fourier integral the above expression can be written as follows

$$\begin{aligned} p_r(t) &\simeq \frac{e^{-i\pi/4}}{2R}\sum_{m=1}^{M}\frac{S(\hat{\omega}_m)\varphi_m(\hat{\omega}_m;z_s)\varphi_m(\hat{\omega}_m;z_r)}{\sqrt{k_m(\hat{\omega}_m)\left|\partial^2 k_m(\hat{\omega}_m)/\partial\omega^2\right|}}e^{i(-k_m(\hat{\omega}_m)R+\hat{\omega}_m t-\delta_m\pi/4)} \\ &= \sum_{m=1}^{M} A_m e^{i(-k_m(\hat{\omega}_m)R+\hat{\omega}_m t-\delta_m\pi/4)} \end{aligned} \tag{17}$$

where $\hat{\omega}_m$ is the stationary point for mode m satisfying the condition

$$\frac{\partial k_m}{\partial\omega}(\hat{\omega}_m) = \frac{t}{R}\,, \tag{18}$$

and $\delta_m = \mathrm{sign}\left(\partial^2 k_m(\hat{\omega}_m)/\partial\omega^2\right)$. Thus, the stationary circular frequency is a function of time $\hat{\omega}_m = \hat{\omega}_m(t)$ and its variation with time is given by the relation

$$\frac{\partial^2 k_m}{\partial\omega^2}d\hat{\omega}_m = \frac{dt}{R}\,. \tag{19}$$

For ray-like arrivals, the contributing wavenumbers $k_m(\hat{\omega}_m)$ at the corresponding stationary points $\hat{\omega}_m$ can be expressed to the 1st order as follows

$$\begin{aligned} k_m(\hat{\omega}_m) &= k_n(\hat{\omega}_n) + \frac{\partial k_m}{\partial m}(m-n) + \frac{\partial k_m}{\partial \omega}(\hat{\omega}_m - \hat{\omega}_n) \\ &= k_n(\hat{\omega}_n) - \frac{2\pi}{D}(m-n) + \frac{t}{R}(\hat{\omega}_m - \hat{\omega}_n) \;\Rightarrow \\ -k_m(\hat{\omega}_m)R + \hat{\omega}_m t &= -k_n(\hat{\omega}_n)R + \hat{\omega}_n t + \frac{2\pi(m-n)R}{D} \end{aligned} \tag{20}$$

where n is selected such that the corresponding stationary point $\hat{\omega}_n$ is close to the central circular frequency ω_0, i.e. $\hat{\omega}_n \approx \omega_0$. Substituting the expression (20) into the stationary phase expression we obtain

$$p_r(t) = e^{i(-k_n(\hat{\omega}_n)R + \hat{\omega}_n t)} \sum_{m=1}^{M} A_m e^{i\left(\frac{2\pi(m-n)R}{D} - \delta_m \pi/4\right)} \tag{21}$$

The time varying part of the phase of the acoustic pressure is

$$\Phi(t) = -k_n(\hat{\omega}_n)R + \hat{\omega}_n t\,, \tag{22}$$

and its time derivative becomes

$$\begin{aligned} \frac{d\Phi(t)}{dt} &= -R\frac{\partial k_n}{\partial \omega}(\hat{\omega}_n)\frac{d\hat{\omega}_n}{dt} + \frac{d\hat{\omega}_n}{dt}t + \hat{\omega}_n \\ &= -R\frac{\partial k_n}{\partial \omega}(\hat{\omega}_n)\frac{1}{R\dfrac{\partial^2 k_m}{\partial \omega^2}} + \frac{1}{R\dfrac{\partial^2 k_m}{\partial \omega^2}}t + \hat{\omega}_n \\ &= \frac{1}{\dfrac{\partial^2 k_m}{\partial \omega^2}}\left(\frac{t}{R} - \frac{\partial k_n}{\partial \omega}(\hat{\omega}_n)\right) + \hat{\omega}_n \\ &= \hat{\omega}_n \approx \omega_0 \end{aligned} \tag{23}$$

In the above expressions the derivative $d\hat{\omega}_n/dt$ has been replaced using eq. (19), and the last line was obtained using the stationary phase condition, eq. (18). The demodulated phase results after removal of the central (carrier) frequency $\tilde{\Phi}(t) = \Phi(t) - \omega_0 t$. The time derivative of the demodulated phase then becomes

$$
\begin{aligned}
\frac{d\tilde{\Phi}(t)}{dt} &= -R\frac{\partial k_n}{\partial \omega}(\hat{\omega}_n)\frac{d\hat{\omega}_n}{dt} + \frac{d\hat{\omega}_n}{dt}t + \hat{\omega}_n - \omega_0 \\
&= -R\frac{\partial k_n}{\partial \omega}(\hat{\omega}_n)\frac{1}{R\dfrac{\partial^2 k_m}{\partial \omega^2}} + \frac{1}{R\dfrac{\partial^2 k_m}{\partial \omega^2}}t + \hat{\omega}_n - \omega_0 \\
&= \frac{1}{\dfrac{\partial^2 k_m}{\partial \omega^2}}\left(\frac{t}{R} - \frac{\partial k_n}{\partial \omega}(\hat{\omega}_n)\right) + \hat{\omega}_n - \omega_0 \\
&= \hat{\omega}_n - \omega_0 \approx 0
\end{aligned}
\tag{24}
$$

Thus the demodulated phase is expected to be close to stationary at the times of ray arrivals.

Phase behavior in different propagation conditions

Fig. 8 shows the arrival pattern and the demodulated phase (2π, i.e. modulo 180°) as functions of time for a Gaussian pulse of central frequency 100 Hz and 3-dB bandwidth 50 Hz, 100 and 300 km away from the source in the environment of Fig. 1. The stationarity of the phase during the early arrivals in the 100-km case can be clearly seen in this figure. The early arrivals are grouped in triplets, and each one of them corresponds to a distinct eigenray connecting source and receiver (the higher arrival in the middle of each triplet group corresponds to 2 symmetric eigenrays). Later arrivals are closer to each other and start overlapping, and as a consequence they are characterized by larger variability of the phase. This behavior is observed also in the 300-km case with the difference of increasing variability of the phase also during the early arrivals.

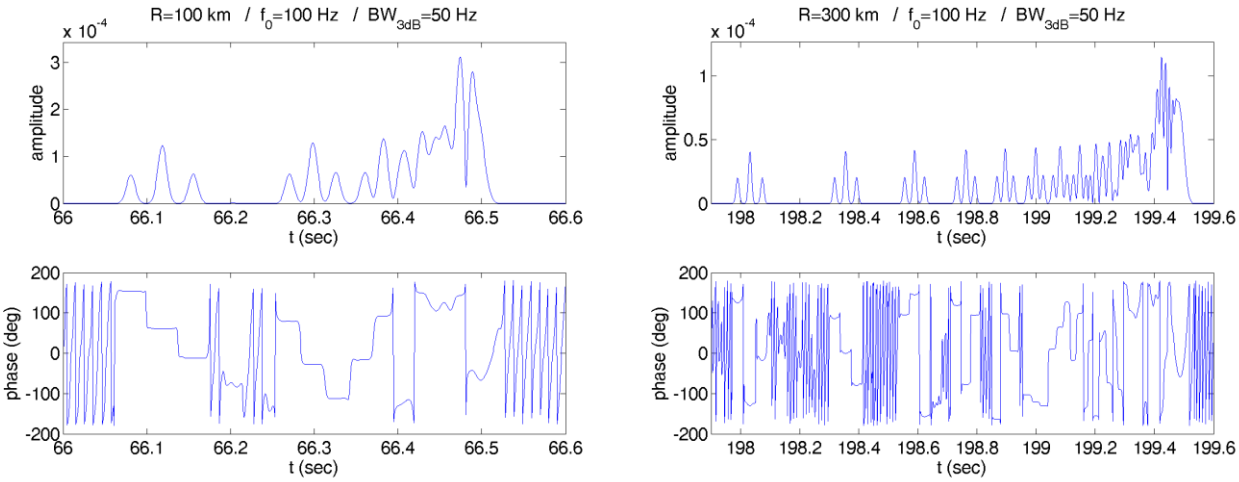

Fig. 8. Arrival pattern and demodulated phase for 100-km and 300-km propagation in the Mediterranean environment, for a 100-Hz pulse with 50-Hz bandwidth.

Fig. 9 shows the arrival pattern and the demodulated phase as functions of time for propagation ranges of 100 and 300 km for a pulse with reduced bandwidth, equal to 10 Hz (3-dB bandwidth). In this case the pulse has a time duration of ~0.1 s such that the arrivals within each triplet of Fig. 8 overlap with

each other. The consequence is that each triplet appears as a single arrival in Fig. 9. The phase during each "triplet" arrival is non-stationary due to the interference of the phases of the underlying ray-like arrivals. The resulting phase in Fig. 9 appears to be a smoothed version of the phases shown in Fig. 8. This behavior of the phase in the case of overlapping ray-like arrivals, suggests that the phase variability of the late arrivals in Fig. 8 is caused by the congestion and overlapping of ray-like arrivals.

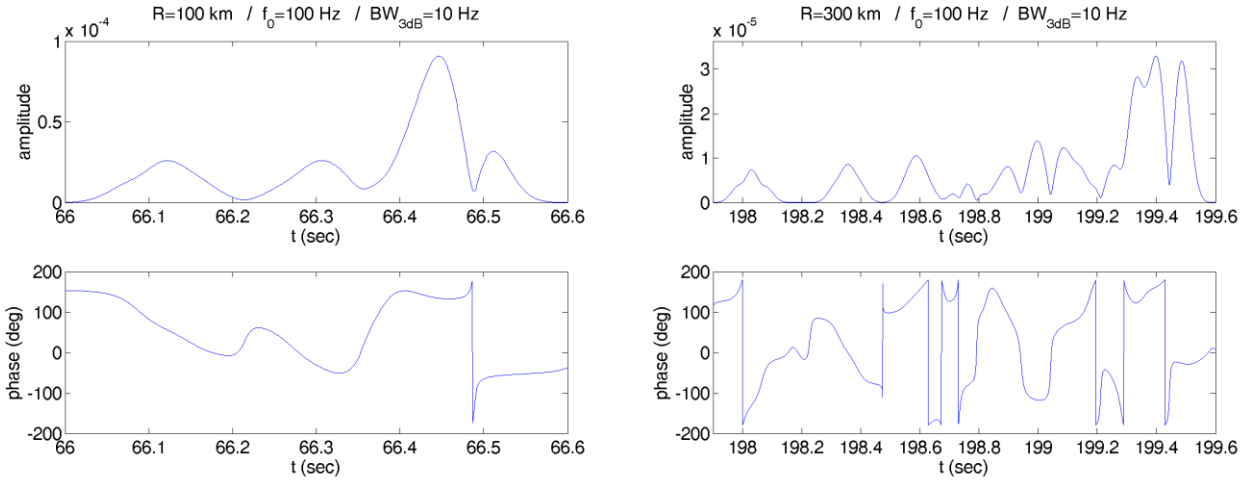

Fig. 9. Arrival pattern and demodulated phase for 100-km and 300-km propagation in the Mediterranean environment, for a 100-Hz pulse with 10-Hz bandwidth.

In the following a closer look into early and late arrivals is attempted. Fig. 10 shows on the left a detailed view of the middle arrival of the second triplet in the right hand panel in Fig. 8 and its demodulated phase corresponding to a propagation range of 300 km. This is a clear ray-like arrival corresponding to a double eigenray with lower turning depth 1611.2 m – in the particular environment all eigenrays are surface-reflected. The duration of the arrival of ~20 ms is in agreement with the reciprocal of the 50-Hz 3-dB bandwidth. The phase during this arrival remains nearly constant (stationary) as can be seen from the lower panel.

Two results are shown in each panel of Fig. 10. The exact ones based on standard normal-mode calculations, represented by the blue lines, and the stationary-phase approximation (described in the previous section), represented by the red dashed lines. It is seen that the results from the two calculations can be hardly discriminated from each other. On the right hand side Fig. 10 shows the corresponding arrival with the same turning depth (1611.2 m) at a 5-fold range of 1500 km. Since the 1500-km double eigenray contain 5 full 300-km eigenrays the resulting time should be the 5-fold of the 300-km arrival time. This is exactly the case in Fig. 10. Further, while the peak arrival preserves its shape in agreement with the used signal bandwidth (50 Hz) the phase (lower panel) exhibits some variability away from the arrival peak. Nevertheless, in both cases the phases is nearly stationary at the peak arrival time, which means similar peak and demodulated phase arrival behavior.

Fig. 11 shows a detailed view of the same arrivals in the case that the signal has a smaller bandwidth (10 Hz) and thus longer duration (~100 ms). In this case the arrival in the middle of the triplet overlaps with the two side arrivals and the phase is the result of superposition. Since the phase of the three ray-like arrivals in each triplet are constant but different, cf. Fig. 8, their interference gives rise to a composite phase that changes with time, i.e. it is non-stationary, which means different peak and

demodulated phase arrival behavior. Thus, the bandwidth appears to be a control factor for the similarity/dissimilarity between peak and phase arrival time perturbation behavior.

Two types of results are shown in Fig. 11, those based on exact normal-mode calculations (blue line) and those calculated from 2-order Taylor expansion of eigenvalues and eigenfunctions [2] about the central source frequency (100 Hz) – narrowband approximation. The agreement between the two is remarkable. The Taylor-expansion method captures the frequency dependence of eigenvalues and eigenfunctions which affects both the phase and the amplitude of each modal component. This allows the isolation of each effect.

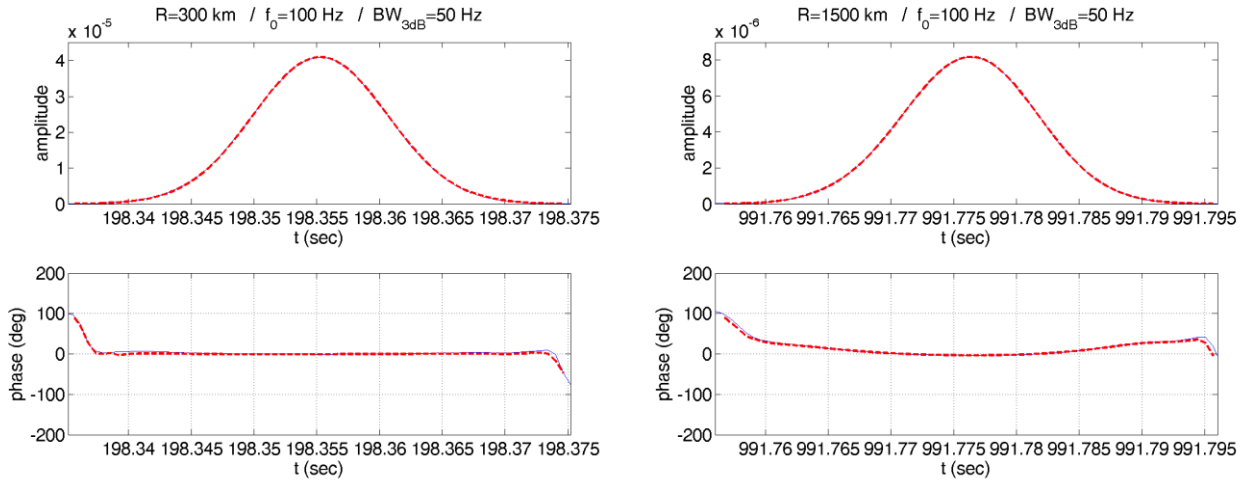

Fig. 10. Early arrival and demodulated phase for 100-km and 1500-km propagation in the Mediterranean environment, for a 100-Hz pulse with 50-Hz bandwidth. The solid blue lines represent the exact normal-mode result and the red dashed lines the stationary phase result.

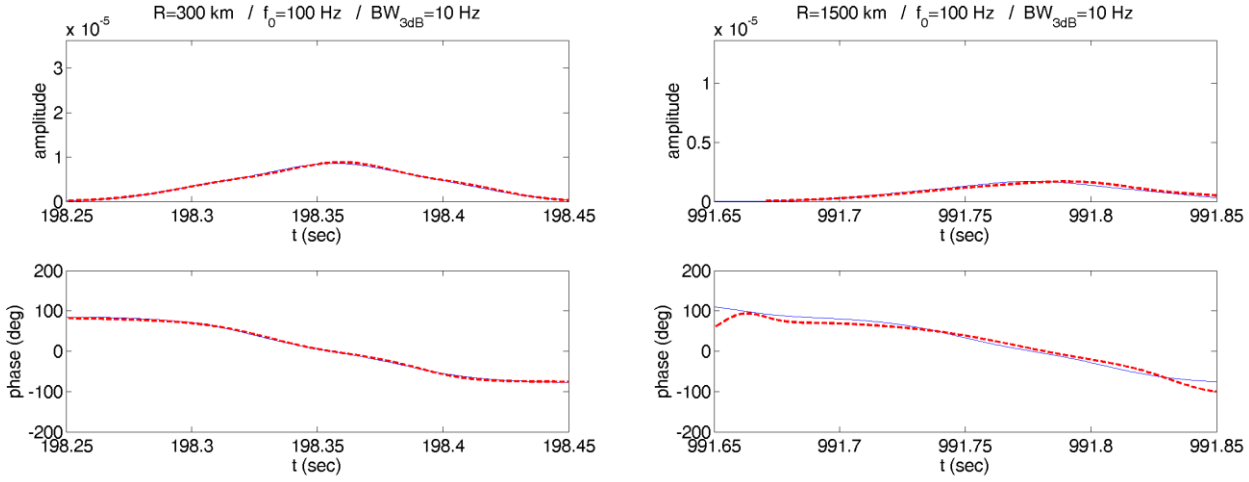

Fig.11 . Early arrival and demodulated phase for 300-km and 1500-km propagation in the Mediterranean environment, for a 100-Hz pulse with 10-Hz bandwidth. The solid blue lines represent the exact normal-mode result and the red dashed lines the result based on 2-order Taylor expansion.

Fig. 12 shows on the left a detailed view of the 300-km late part of the arrival pattern shown in Fig. 8. The solid blue lines represent the exact normal-mode result and the red dashed lines the stationary phase result. A very good agreement is observed over the signal duration. Ray resolvability is no longer apparent in this part of the arrival pattern, whereas the phase is characterized by large variability – the phase still exhibits stationary points (local maxima or minima) at certain time instants, which however do not correspond to peak arrival times. Late arrivals can in general be represented by a small number of low order modes. The right-hand panels in Fig. 12 show the corresponding late arrival pattern for propagation range 1500 km. In this case, a large number of peaks is observed, caused by mode interference. The three main lobes under the peak multiplicity correspond to the first 3 modes of propagation. During these lobes the phase exhibits near-stationary points with superposed alternations.

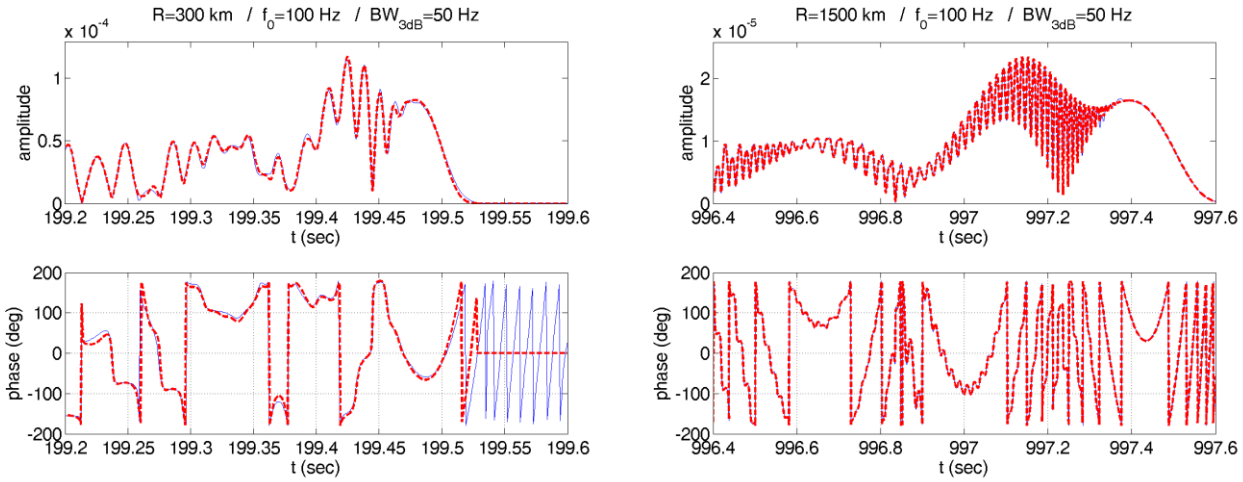

Fig. 12. Late arrivals and demodulated phase for 100-km and 1500-km propagation in the Mediterranean environment, for a 100-Hz pulse with 50-Hz bandwidth. The solid blue lines represent the exact normal-mode result and the red dashed lines the stationary phase result.

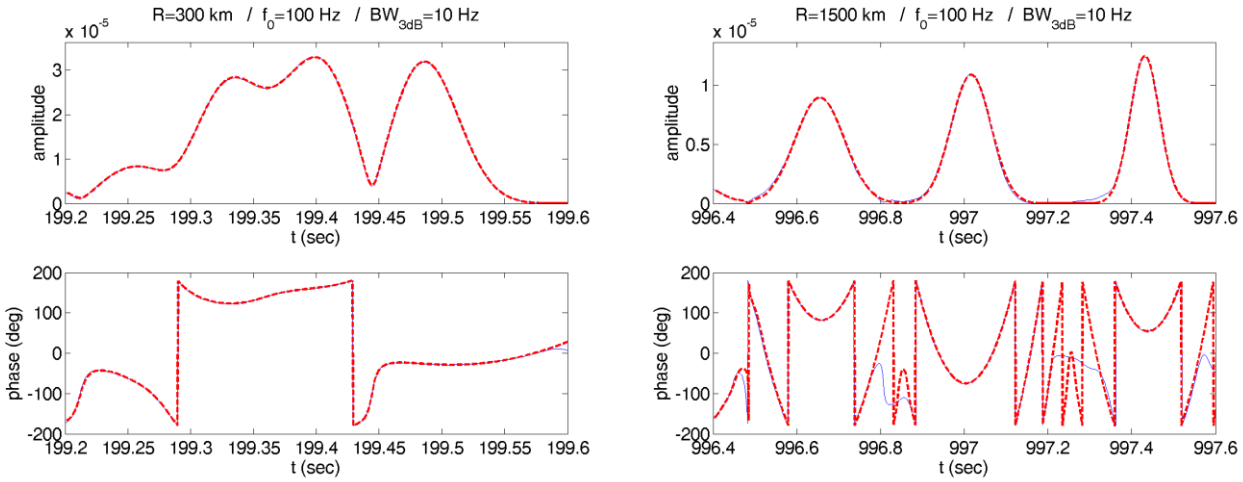

Fig. 13. Late arrivals and demodulated phase for 300-km and 1500-km propagation in the Mediterranean environment, for a 100-Hz pulse with 10-Hz bandwidth. The solid blue lines represent the exact normal-mode result and the red dashed lines the result based on 2-order Taylor expansion.

The three modes of propagation are more clearly seen in Fig. 13 where the signal bandwidth is reduced to 10 Hz. In this figure the results based on exact normal-mode calculations are represented by the blue line. The red dashed lines represent results from the 2-order Taylor expansion of eigenvalues and eigenfunctions about the central source frequency (100 Hz) – narrowband approximation. The agreement between the two is remarkable in all cases. In Fig. 13 the last peak corresponds to the first mode of propagation, the last but one to mode 2 and the previous peak to mode 3. While these peaks are well separated at the range of 1500 km, Fig. 13 on the right, they overlap with each other at the range of 300 km, especially modes 2 and 3. In the case of separate arrivals the phase exhibits stationary points that appear to be close to the corresponding peaks, whereas in the case of overlapping modes the stationarity is lost, as in the case of overlapping ray arrivals seen before.

Fig. 14 shows a detailed view of the last peak arrival corresponding to mode 1 and its phase for the ranges of 300 and 1500 km, respectively. Three types of results are shown on each panel: exact normal-mode results (blue lines), results based on the 2-order Taylor expansion of eigenvalues and eigenfunctions in the phase and amplitude of modal components (red dashed lines), and results based on the 2-order Taylor expansion of eigenvalues in the phase only (green dashed lines). From this figure it is seen that in the exact results (blue lines) the phase minimum (stationary point) does not coincide with the peak arrival time. A similar thing happens in the case of the full Taylor expansion (red dashed lines), which gives a good approximation to the exact results. Nevertheless, when the Taylor expansion is limited to the phase only (green dashed lines) the phase stationary point coincides with the peak arrival time. This indicates that the frequency dependence of the modal excitation is enough to cause differentiation between peak and demodulated phase arrival times even in the case of isolated modal arrivals. On the other hand, the phase at the peak arrival time though not exactly stationary is nearly stationary, which points to small deviation in the perturbation behavior between peak and demodulated phase arrival times. In the case of overlapping modes, as in the case of modes 2 and 3 for propagation range 300-km in Fig. 13, the phase is non-stationary due to interference. Thus isolated ray-like or modal arrivals appear to be characterized by near-stationarity of the phase at the peak arrival time. When these arrivals overlap with each other, due to narrow bandwidth or short propagation range, different phase values interfere and give rise to non-stationarity.

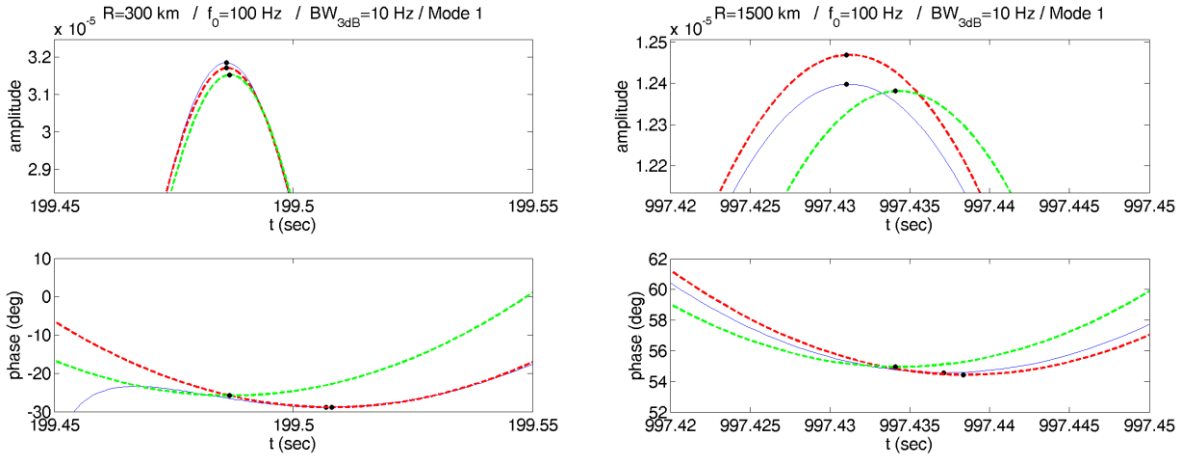

Fig. 14. Amplitude and demodulated phase near the cutoff for 300-km and 1500-km propagation in the Mediterranean environment, for a 100-Hz pulse with 10-Hz bandwidth. The solid blue lines represent the exact normal-mode result, the red dashed lines the result based on 2-order Taylor expansion, and the green dashed lines the result based on Taylor expansion of the phase only.

Some results for different environments are shown in the following. Fig. 15 shows a temperate sound-speed profile typical for the North Pacific Ocean, with axial depth (sound-speed minimum) at 1100 m, in a 5400-m deep water layer, followed by an absorbing bottom half space. Source/receiver are assumed at axial depth 1100 m.

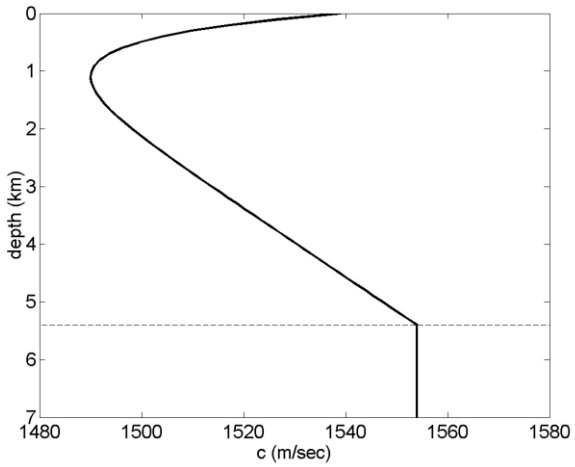

Fig. 15. Typical North Pacific sound-speed profile.

Fig. 16 presents the arrival pattern and the demodulated phase as functions of time for propagation of a Gaussian pulse of central frequency 100 Hz and 3-dB bandwidth 50 Hz over ranges of 100 and 300 km. The triplet structure is clearly seen in the longer-range result. In both cases the early arrivals correspond to single eigenrays, and the phase is near-stationary. The last arrival is the result of superposition of a large number of modes (about 50 modes). Its phase is stationary in the 100-km case and non-stationary in the 300-km case, pointing to significant differentiation in the behavior of the underlying modal components in the latter case. A detailed view of an early arrival as well as the last arrival and its phase for propagation range of 300 km is given in Fig. 17. .

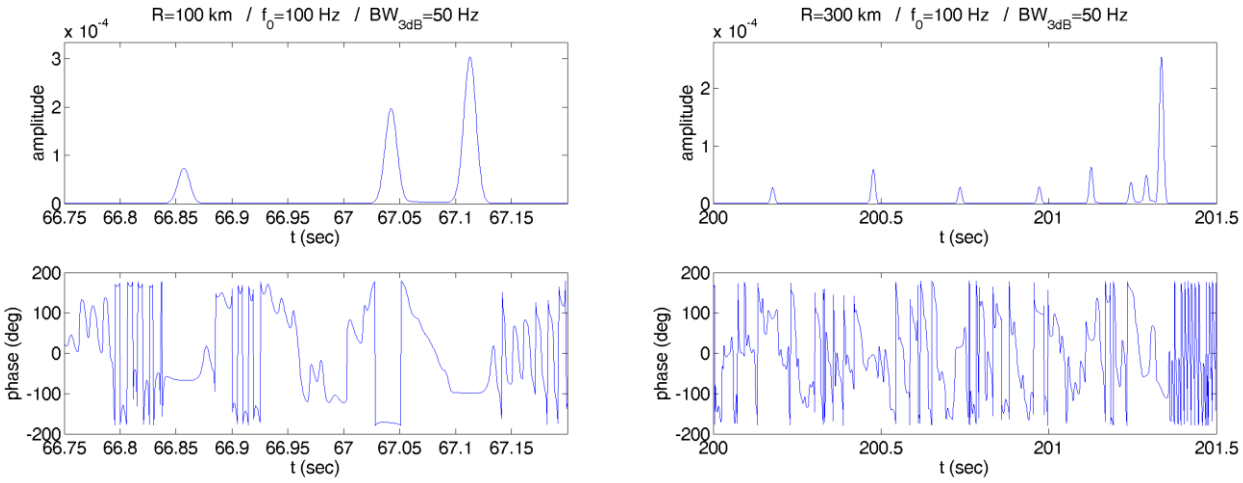

Fig. 16. Amplitude and demodulated phase for 100-km and 300-km propagation in the North Pacific environment, for a 100-Hz pulse with 50-Hz bandwidth.

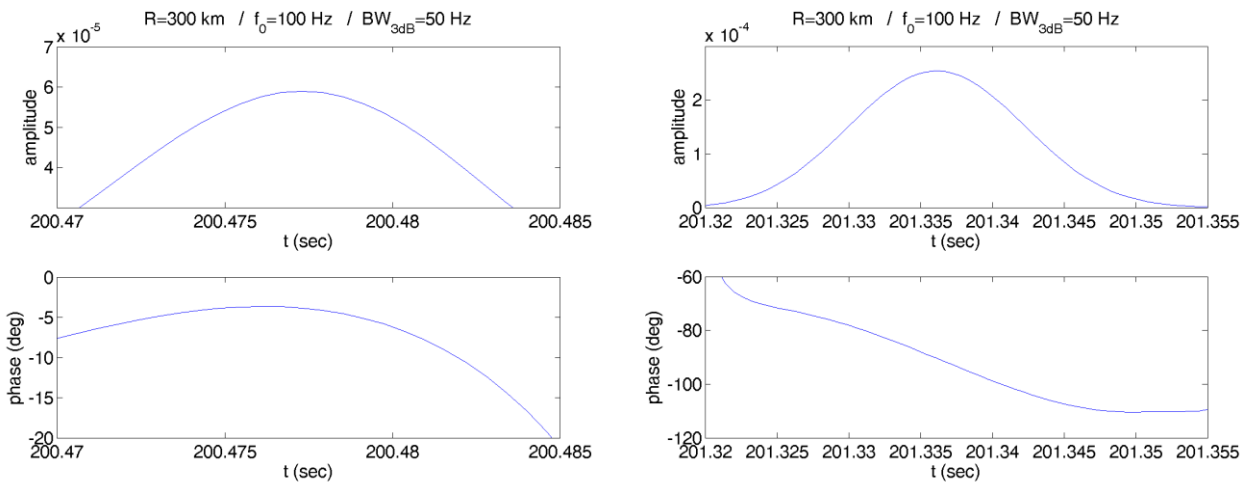

Fig. 17. Detail: Early arrival (left) and late arrival (right) amplitude and demodulated phase for 300-km propagation in the North Pacific environment, for a 100-Hz pulse with 50-Hz bandwidth.

Fig. 18 describes a shallow-water environment, a Pekeris waveguide. The water depth is 200 m and the sound speed in the water is taken 1500 m/s. The bottom is taken to be a half space of sound speed 1900 m/sec. Source and receiver are assumed at a depth of 50 m – dots in Fig. 18 – and horizontal distance of 3 km. The acoustic signal is a Gaussian pulse with bandwidth 50 Hz (3-dB bandwidth).

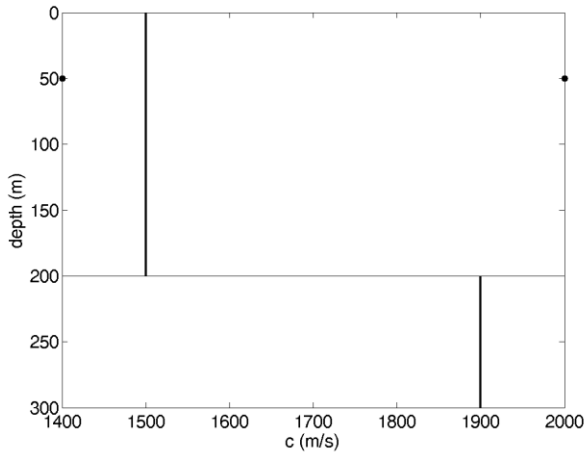

Fig. 18. Pekeris waveguide

Fig. 19 shows the arrival pattern and the demodulated phase at a range of 3 km for two values of the central frequency of the Gaussian pulse, 150 Hz and 300 Hz. The arrival pattern in this case, opposite to deep-water propagation, starts with near-horizontal arrivals corresponding to low-order modes and continues with gradually steeper arrivals, with increasing separation, until the critical angle is reached. Later arrivals are ray-like corresponding to single (or double symmetric) eigenrays and are grouped in triplets. Three such triplets are clearly seen in Fig. 19, during which the phase attains stationarity at the peak arrival times of the constituent arrivals. The early arrivals are the result of superposition of more than one ray/modal arrivals and in this connection the phase is variable. In Fig. 20 the stationary phase

prediction (red dashed lines) is superposed to the exact normal-mode results (blue lines). It is seen that the agreement in the amplitude and especially in the phase is better in the higher-frequency (300-Hz) case. Early arrivals cannot be well represented in the stationary-phase approximation due to the limited dispersion of the low-order modes.

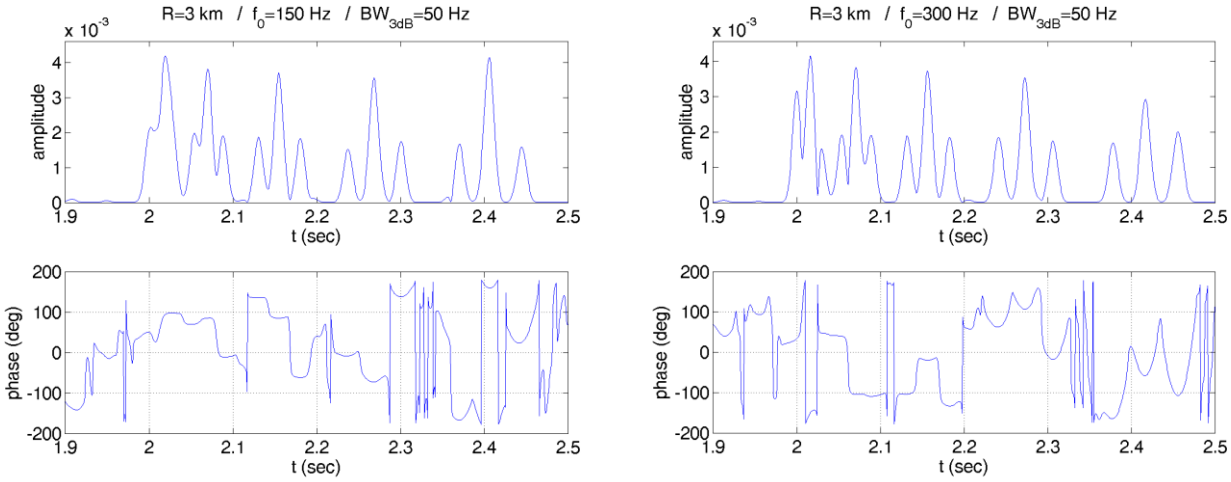

Fig. 19. Amplitude and demodulated phase for 3-km propagation in the Pekeris shallow water waveguide, for a 150-Hz and 300-Hz pulse with 50-Hz bandwidth.

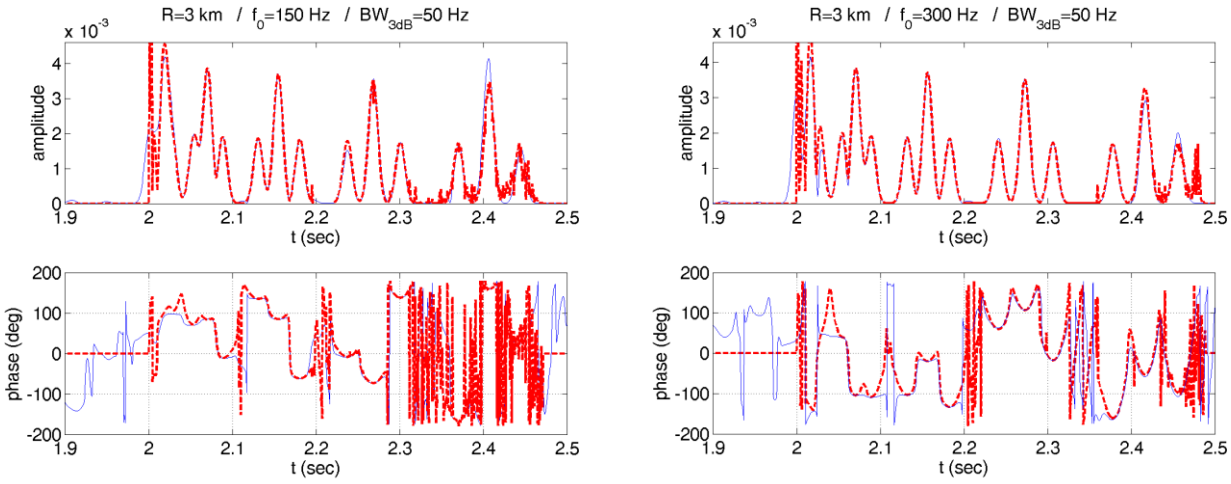

Fig. 20. Amplitude and demodulated phase for 3-km propagation in the Pekeris shallow water waveguide, for a 150-Hz and 300-Hz pulse with 50-Hz bandwidth. The solid blue lines represent the exact normal-mode result and the red dashed lines the stationary phase result.

In the following the behavior of the arrival pattern and the phase in the vicinity of turning points is considered. The results shown are for the linear sound-speed profile shown in Fig. 1. As already mentioned the early arrival focused on in Fig. 10 is a ray-like arrival corresponding to a double symmetric eigenray connecting source and receiver with turning depth 1611.2 m. One of these eigenrays is shown in Fig. 21 for the range of 300 km; it departs from the source on the left at 150 m depth with downward direction and arrives to the receiver on the right at 150 m depth from the above (both launch and arrival grazing angles are negative). This eigenray has 9 lower turning points, whose ranges and corresponding arrival times are summarized in Table 1. In the following the focus is on the last turning point with range ~282545 m and travel time 186.8021 s.

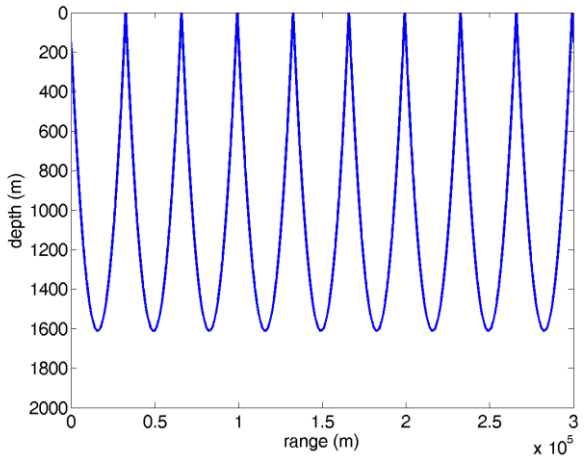

Fig. 21. Eigenray corresponding to the arrival of Fig. 10 in the Mediterranean environment with turning depth 1611.2 m for range 300 km.

Table 1. Range and corresponding arrival time of the 9 lower turning points of Fig. 21 with turning depth 1611.2 m

Range (m)	*Arrival time (s)*
15878.7943	10.4866
49212.1366	32.526
82545.4789	54.5655
115878.8212	76.6049
149212.1636	98.6443
182545.5059	120.6838
215878.8482	142.7232
249212.1905	164.7627
282545.5328	186.8021

Fig. 22 shows the time-front diagram for this range and source depth 150 m, with the horizontal axis measuring arrival time and the vertical axis measuring receiver depth. For receiver depth equal to the source depth (150 m) the triplet structure is seen, in which each triplet corresponds to two single eigenrays (side arrivals) and two symmetric eigenrays with identical travel time (double arrival in the middle). For other receiver depths the symmetry is lost and triplets are replaced by groups of 4 arrivals. As the receiver goes deeper arrivals from different groups get closer to each other and at certain receiver depths they form new triplets. As the receiver further descends these triplets are again replaced by groups of 4 arrivals which finally coalesce in groups of two as the corresponding turning depth is reached. As the receiver goes deeper late arrivals are stripped off simply because the receiver lies deeper than their lower turning depth. In Fig. 22 the focus is on the ray with turning depth 1611.2 m. In this connection four horizontal lines are drawn in the figure representing receiver depths 1310, 1510, 1610, and 1710 m.

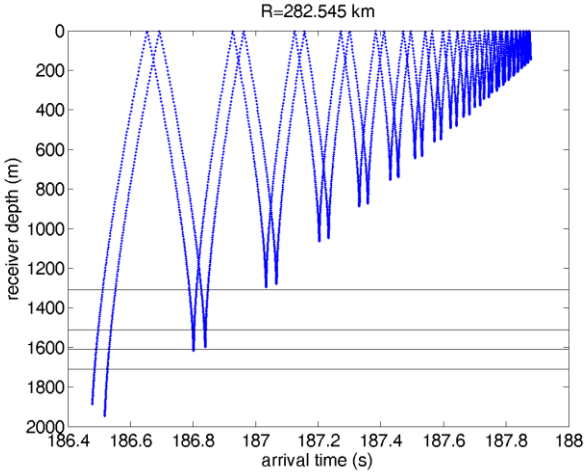

Fig. 22. Time-front diagram for the Mediterranean sound-speed profile at 282545-m range for source depth 150 m.

Fig. 23 shows the normal-mode prediction (arrival pattern and demodulated phase) of a Gaussian pulse of central frequency 100 Hz and 3-dB bandwidth 50 Hz for range 282545 m, source depth 150 m, and receiver depths 1310, 1510, 1610, and 1710 m, respectively. The wave-theoretic arrival structure corresponds to the ray-theoretic prediction shown in Fig. 22: At a depth of 1310 m a group of 4 arrivals is seen at the right arrival times. Then, at the depth of 1510 m these arrivals coalesce in two groups of two; the degree of coalescence of the last two is higher (being closer to the corresponding slightly shallower turning depth, cf. Fig. 22) and thus the corresponding last arrival amplitude is higher than that of the previous arrival. At the depth of 1610 m it is the other way round, the first arrival is higher due to the fact that the depth coincides with the lower turning depth of the corresponding rays whereas it is deeper than the turning depth of the subsequent rays which thus fade out. Finally the depth of 1710 m lies deeper than the turning depth of the 4 eigenrays. The wave-theoretic arrivals are still to see, however they are weaker. Concerning the phase, as long as the wave theoretic arrivals are ray-like, i.e. they correspond to a single eigenray each, the phase is close to stationary during each arrival, as is seen in the case of receiver depth equal to 1310 m, away from the lower turning depth. In the case of overlapping between different ray arrivals as is the case of depths in the neighborhood of the turning depths the phase becomes non-stationary.

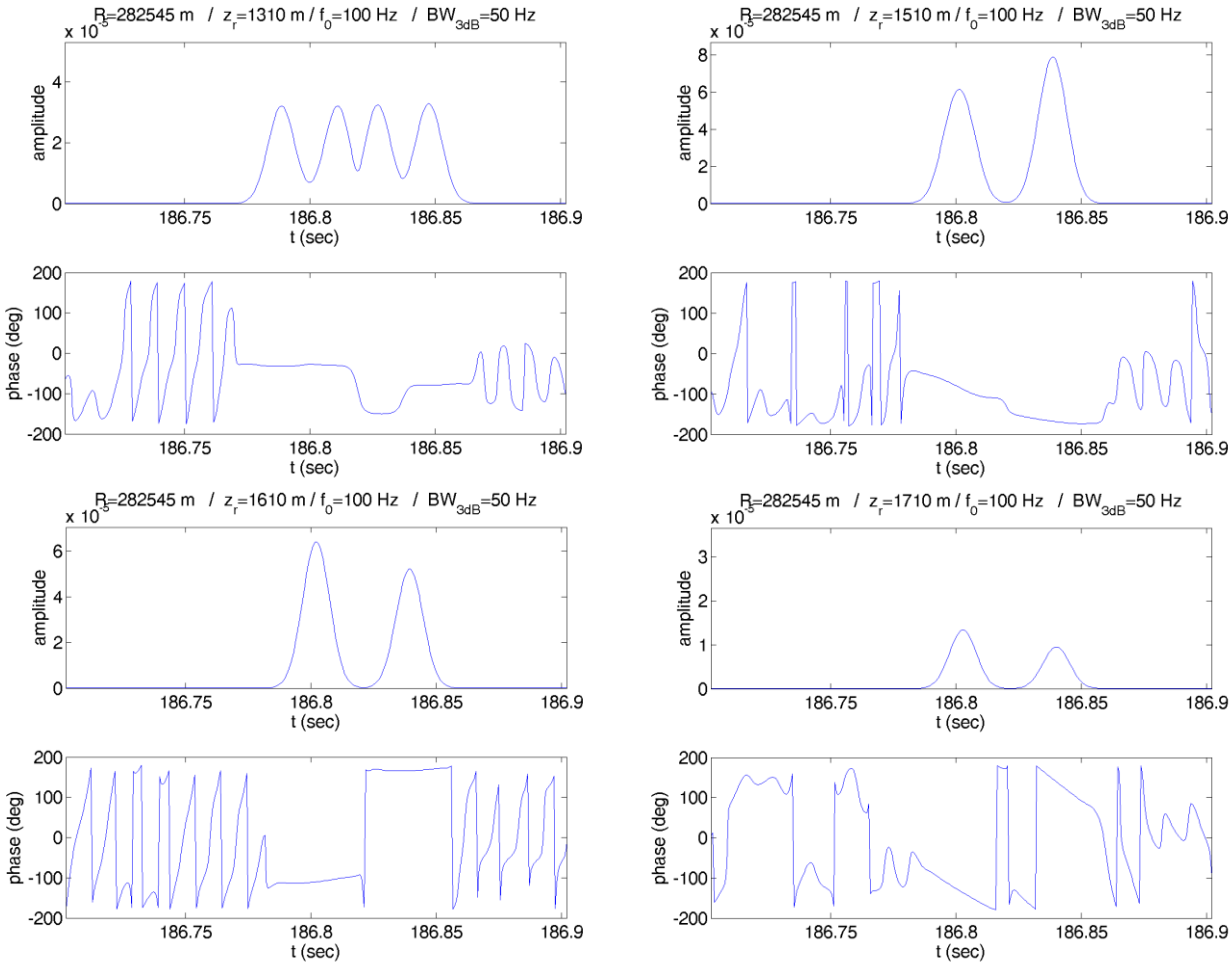

Fig. 23. Arrival pattern and demodulated phase for a 100-Hz pulse with 50-Hz bandwidth at a range of 282545 m and depths 1310, 1510, 1610, and 1710 m.

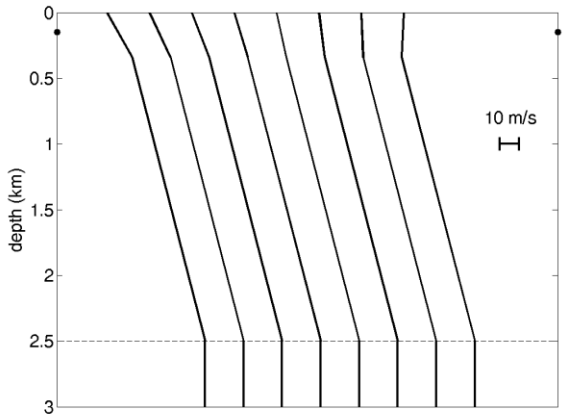

Fig. 24. Range-dependent linear sound-speed profiles.

The behavior of the phase in the presence of range dependence is considered next. The linear sound-speed profile of Fig. 1 with a superposed range-dependent perturbation is shown in Fig. 24. The perturbation is confined in the upper layer, shallower than 340 m, and spans 14 m/s at the surface, linearly decreasing to zero at 340-m depth. Source and receiver are assumed at a depth of 150 m, marked by dots in Fig. 24. Fig. 25 on the left shows the arrival pattern and the demodulated phase as functions of time for a Gaussian pulse of central frequency 100 Hz and 3-dB bandwidth 50 Hz 300 km away from the source in the above range-dependent environment. For these calculations the source-receiver range has been divided into 8 range segments of equal size, each one with constant sound-speed profile, as shown in Fig. 24. Results from exact coupled-mode and adiabatic calculations, black and blue lines, respectively, are shown in this figure. It is seen that there are differences between the two calculations both in the early and the late part of the receptions, both in the arrival pattern (amplitude) and the phase. The early arrival triplet structure is recognized in both calculations. Even though mode coupling affects the arrival amplitudes early arrivals the corresponding arrival times are in agreement. The phase appears to be near-stationary during some early peaks and non-stationary during others, especially during the peaks in the middle of the triplets; an explanation is given below. Mode coupling becomes stronger in the case of late arrivals sensing layers between the surface and gradually shallower depths and thus subject to the range dependence to a larger degree. In this case both amplitudes and arrival times are affected. The right-hand panels in Fig. 25 show the corresponding results for a narrowband Gaussian pulse of central frequency 100 Hz and 3-dB bandwidth 10 Hz. The early triplets have been replaced by single broad peaks resulting from the superposition of adjacent arrivals. The phase is variable along these peaks as in the range-independent case.

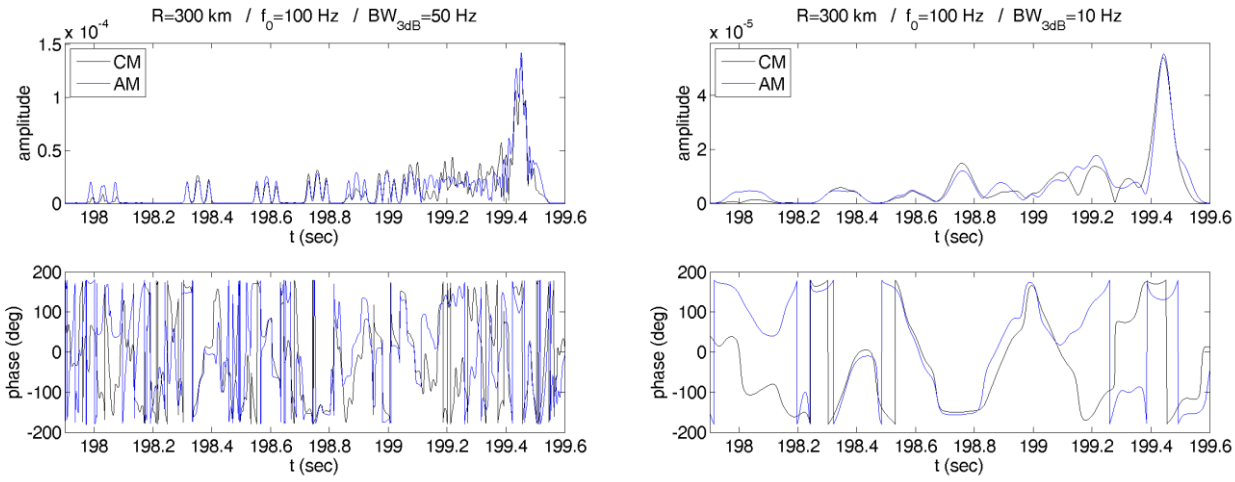

Fig. 25. Arrival pattern and demodulated phase for 300-km propagation in the range-dependent Mediterranean environment, for a 100-Hz pulse with 50-Hz (left) and 10-Hz (right) bandwidth. Black lines represent coupled-mode (CM) results and blue lines adiabatic-mode (AM) results.

Fig. 26 presents a detailed view of the amplitude and phase of the early triplet about 198.35 s. for bandwidth 50 Hz on the left and 10 Hz on the right. On the left-hand panels it is seen that the side arrivals of the triplet are characterized by near-stationary phase whereas the phase during the one in the middle is clearly non-stationary. This is because the middle arrival is a double arrival, which in the range-independent case for equal source and receiver depths (150 m) would correspond to two symmetric eigenrays. In the range-dependent case considered here, the symmetry is broken and the two

underlying eigenrays are different. In this connection the middle peak behaves the same way as in the case of superposition of two different ray-like arrivals (case of reduced bandwidth) each one of them with a different phase, which results in non-stationarity of the composite phase. The right-hand panels in Fig. 26 show exactly this at the triplet level. When the bandwidth is narrow the triplet is replaced by a single broad peak, a smoothed version of the triplet, and the phase is non-stationary due to superposition of the underlying ray-like peaks with constant but different phase each.

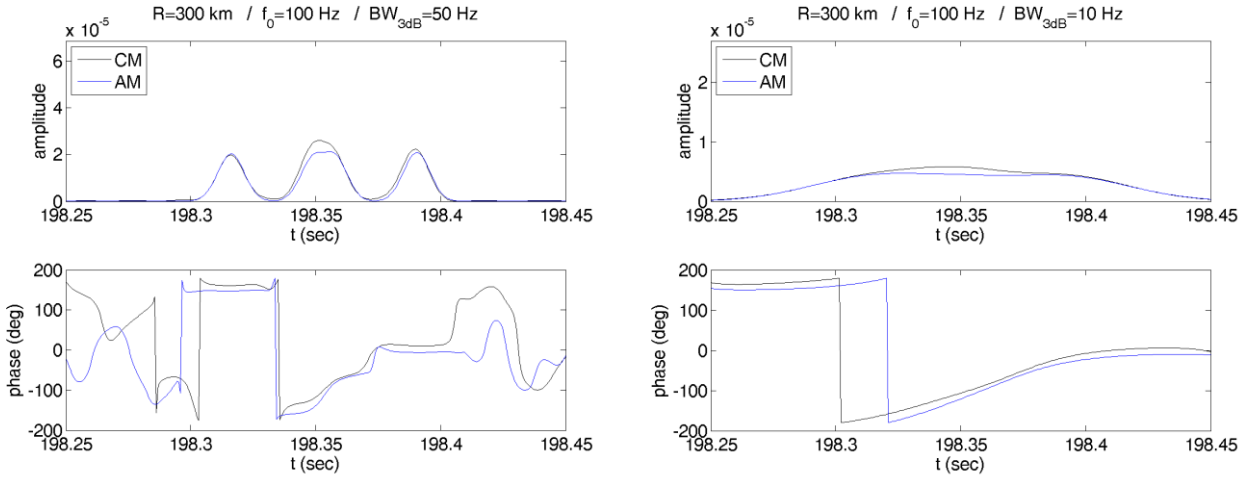

Fig. 26. Early arrivals and demodulated phase for 300-km propagation in the range-dependent Mediterranean environment, for a 100-Hz pulse with 50-Hz (left) and 10-Hz (right) bandwidth. Black lines represent coupled-mode (CM) results and blue lines adiabatic-mode (AM) results.

Fig. 27 presents a detailed view of the amplitude and demodulated phase of the late arrivals in the range-dependent environment for bandwidth 50 Hz on the left and 10 Hz on the right. In the broadband case on the left there is a multitude of peaks which are the result of mode interference. As already mentioned these arrivals correspond to gradually shallower eigenrays (spanning layers from the surface to gradually shallower depths) and are thus more exposed to range dependence. In this connection mode coupling is stronger and the difference between coupled and adiabatic mode results is larger. This also applies to the phase whose stationary points clearly do not coincide with the times of the peaks. The situation is smoother in the narrowband case on the right. Three peaks are observed both in the coupled and adiabatic mode calculations whose amplitudes, arrival times and phase are different, however. The phase is close to stationary (still, not exactly stationary) in the case of the last two arrivals. Fig. 28 shows the same results with superposed coupled and adiabatic modes calculations based on 2-order Taylor expansions (fast normal mode – fnm – calculations), red and green dashed lines, respectively. The narrower the bandwidth the better the Taylor approximation works. This is very well seen in Fig. 28. In the broadband case there is significant deviations in the amplitudes even those of the last peaks. Still, there is remarkable agreement in the phase of these peaks. In the narrowband case the approximation performs perfectly well for both amplitudes and phase – the only deviations in the phase appear in the late times, beyond 199.55 s, in the no-signal area.

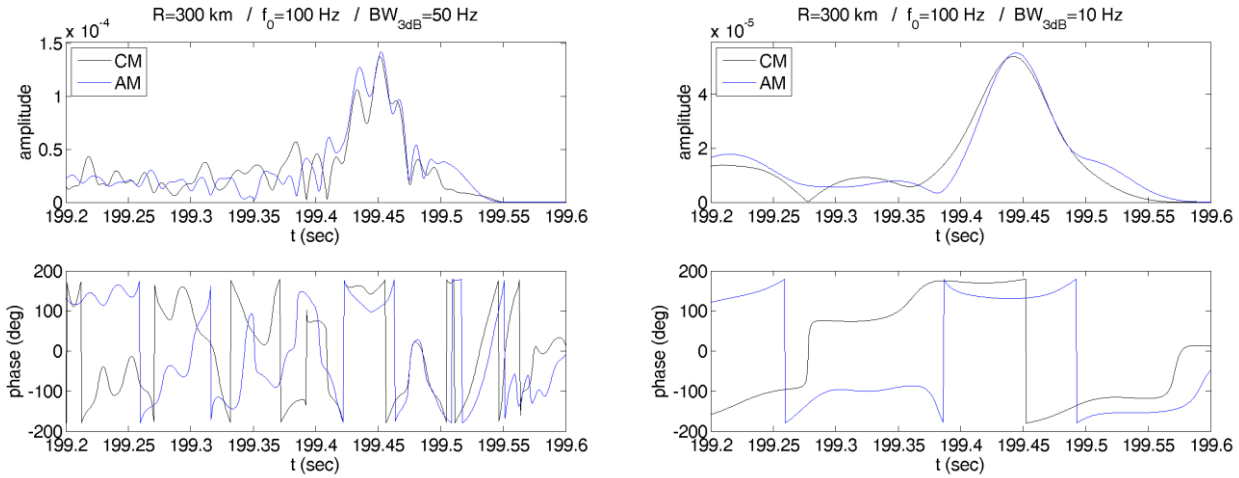

Fig. 27. Late arrivals and demodulated phase for 300-km propagation in the range-dependent Mediterranean environment, for a 100-Hz pulse with 50-Hz (left) and 10-Hz (right) bandwidth. Black lines represent coupled-mode (CM) results and blue lines adiabatic-mode (AM) results.

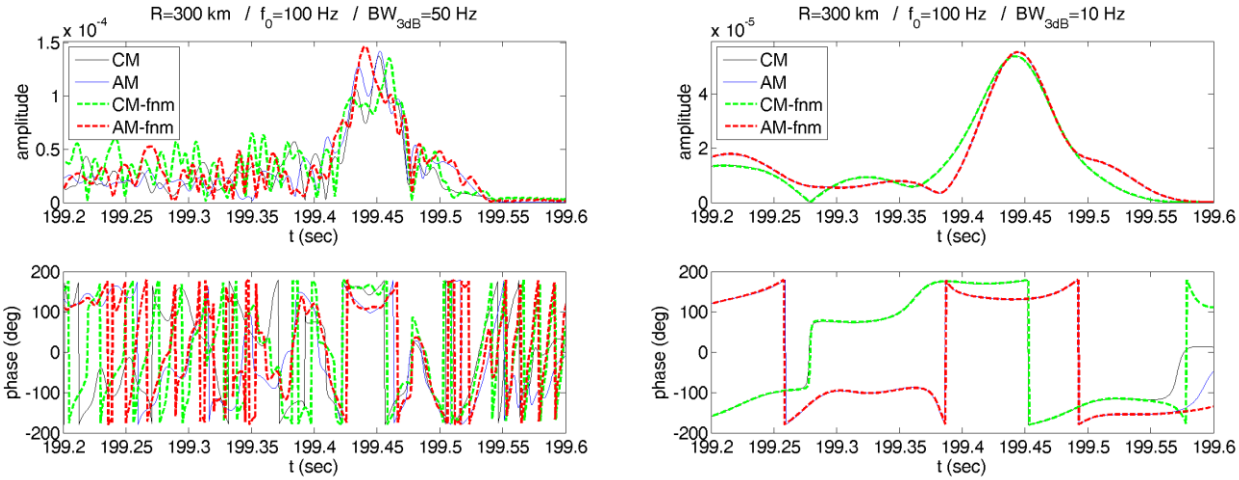

Fig. 28. Late arrivals and demodulated phase for 300-km propagation in the range-dependent Mediterranean environment, for a 100-Hz pulse with 50-Hz (left) and 10-Hz (right) bandwidth. Black lines represent coupled-mode (CM) results and blue lines adiabatic-mode (AM) results. Green and red dashed lines represent corresponding results based on 2-order Taylor expansion (FNM).

IMPACT/APPLICATIONS

The phase of wave-theoretic ray-like arrivals (early arrivals in deep-water propagation and late arrivals in shallow-water propagation) is close to stationary for arrivals corresponding to single eigenrays or symmetric eigenrays, as in the case of arrivals in the middle of arrival triplets in range-independent propagation for equal source-receiver depths. When ray-like arrivals overlap with each other, e.g. in the case of narrowband signals, the resulting phase becomes non-stationary; this is because the phases of the interfering arrivals are constant but different such that their superposition gives rise to non-stationarity, which means different perturbation behavior of corresponding peak and demodulated phase arrivals. This also happens when the symmetry of eigenrays underlying double arrivals is broken, e.g. in the case of range dependence or in the case of range independence and different source and receiver depths. In those cases the ray-theoretic triplets are replaced by quadraplets; if the arrivals in the middle are close enough to each other and give rise to a single peak arrival then the phase along that arrival behaves in a non-stationary way. The same happens in the vicinity of the turning depths, since the correspodning peak arrivals are the result of overlapping between nearby ray-like arrivals. Coming to modal arrivals (late arrivals in deep-water propagation or early arrivals in shallow-water propagation), the phase is stationary at the peak arrival times only in case where the peak arrivals are isolated modal arrivals and frequency dependence of mode amplitudes is negligible. Otherwise, the phase of modal arrivals is becomes non-stationary. This is also the case when mode interference takes place.

REFERENCES

[1] G.N. Makrakis, E.K. Skarsoulis, Asymptotic approximation of ocean-acoustic pulse propagation in the time domain, *J. Comp. Acoustics*, vol. 12, pp. 197-216, 2004.

[2] E.K. Skarsoulis, Second-order Fourier synthesis of broadband acoustic signals using normal modes, *J. Comp. Acoustics*, vol. 5, pp. 355-370, 1997.

[3] E.K. Skarsoulis, Fast Coupled-Mode Approximation for Broadband Pulse Propagation in a Range-Dependent Ocean, *IEEE Journal of Oceanic Engineering*., Vol. 24, pp. 172-182, 1999.

[4] E. Skarsoulis, B. Cornuelle, M. Dzieciuch, Sensitivity behavior of phase and peak arrival times, *Proc. 1st International Conference on Underwater Acoustics*, pp. 1221-1228, Corfu, 2013.

[5] K.M. Guthrie, C.T.Tindle, Ray effects in the normal mode approach in underwater acoustics, *J. Sound Vib*., vol. 47, pp. 403-413, 1976.